

Application of FUN3D Solver for Aeroacoustics Simulation of a Nose Landing Gear Configuration

Veer N. Vatsa^{*}, David P. Lockard[†] and Mehdi R. Khorrami[‡]

NASA Langley Research Center, Hampton, VA 23681

Numerical simulations have been performed for a nose landing gear configuration corresponding to the experimental tests conducted in the Basic Aerodynamic Research Tunnel at NASA Langley Research Center. A widely used unstructured grid code, FUN3D, is examined for solving the unsteady flow field associated with this configuration. A series of successively finer unstructured grids has been generated to assess the effect of grid refinement. Solutions have been obtained on purely tetrahedral grids as well as mixed element grids using hybrid RANS/LES turbulence models. The agreement of FUN3D solutions with experimental data on the same size mesh is better on mixed element grids compared to pure tetrahedral grids, and in general improves with grid refinement.

Nomenclature

BART	Basic Aerodynamic Research Tunnel
BDF	backward differencing formulation
BDF2	second-order backward differencing formulation
BDF2OPT	optimized second-order backward differencing formulation
CFD	computational fluid dynamics
DES	detached eddy simulation
DDES	delayed detached eddy simulation
FW-H	Ffowcs Williams-Hawkings
HRLES	hybrid RANS/LES
LaRC	Langley Research Center
LES	large eddy simulation
MDDDES	modified delayed detached eddy simulation
NLG	nose landing gear
PDCC	partially-dressed closed-cavity
PSD	power spectral density
PIV	particle image velocimetry
RANS	Reynolds-averaged Navier-Stokes
SPL	sound pressure level
SST	shear stress transport
TKE	turbulence kinetic energy
UFAFF	University of Florida Aeroacoustic Facility
URANS	unsteady Reynolds-averaged Navier-Stokes
u, v, w	Cartesian fluid velocity components
x, y, z	Cartesian coordinates
Z-vort	spanwise vorticity

Superscript:

' perturbation quantity (e.g. $u' = u - u_\infty$)

Subscript:

∞ free-stream quantity

^{*}Research Engineer, Computational AeroSciences Branch, Research Directorate; Associate Fellow AIAA

[†]Research Engineer, Computational AeroSciences Branch, Research Directorate; Senior Member AIAA

[‡]Research Engineer, Computational AeroSciences Branch, Research Directorate; Associate Fellow AIAA

I. Introduction

In recent years, there has been growing emphasis on reducing airframe noise to meet the increasingly aggressive standards for permissible noise near airports. The landing gear is a significant contributor to airframe noise during approach and landing for commercial aircraft,¹ and, therefore, it is important to understand the noise sources associated with such configurations. Despite significant progress made in the field of computational fluid dynamics (CFD) during the last several decades, prediction of noise sources around the landing gear of an aircraft is still an extremely challenging problem for CFD practitioners. The geometric complexity and highly chaotic unsteady flow fields associated with landing gear pose numerous difficulties for numerical simulation. Generating suitable point-matched structured grids for such configurations is extremely difficult and a time consuming task, making such an approach somewhat impractical. Hence, earlier structured grid work in this area focused on simplified landing gear configurations.^{2,3} The grid generation task for structured grids can be simplified by using an overset grid approach. However, such approaches in general do not maintain conservation properties across overset zones. Another approach for circumventing grid generation difficulties is to make use of embedded Cartesian grids. Such an approach is used in the PowerFLOW code,⁴⁻⁶ where a discrete Lattice Boltzmann method is coupled to a turbulence model. In addition, this approach uses wall functions at solid walls to reduce the mesh count for practical problems instead of integrating to the wall.

Unstructured grid methodology offers significant advantage in terms of grid generation and has been gaining popularity in the CFD community in recent years with an increasing emphasis on solving unsteady viscous flow over complex configurations, as evidenced by the recent publications appearing in the literature.⁷⁻¹³ For the current work, we make use of a widely-distributed, unstructured-grid flow solver FUN3D,¹⁴ where the Navier-Stokes equations supplemented by turbulence models are solved to simulate the viscous unsteady flow field for configurations of interest. The FUN3D code has been used for many large-scale applications in the past.¹⁴ It was recently applied to solve the unsteady flow past single- and tandem- cylinder configurations,¹⁵ where time-averaged and perturbation quantities were shown to be in fairly good agreement with experimental data and earlier computations from a well-established, structured-grid flow solver CFL3D.¹⁶

In this paper, we focus on simulating the flow over a Gulfstream G550 nose landing gear. A series of successively finer grids has been generated in order to assess the effect of grid induced truncation errors on FUN3D solutions. Based on prior experience in solving unsteady flow over bluff bodies that induce large regions of reverse flow,¹⁵ we make use of a hybrid RANS/LES approach where the RANS equations are solved in the near wall regions surrounded by turbulent boundary layers, and an implicit large eddy simulation (LES) is performed in regions where the grid can resolve the turbulent eddies and unsteadiness. In an implicit LES, the artificial dissipation of the numerical scheme acts as the subgrid scale model. In general with low-order codes, the artificial dissipation is at least as large as what would be prescribed by an explicit model.

II. Experiments

A series of wind tunnel experiments for a 1/4 scale model of a Gulfstream G550 aircraft nose landing gear has been performed in the Basic Aerodynamic Research Tunnel (BART)¹⁷ at NASA Langley Research Center (LaRC) and the University of Florida Aeroacoustic Flow Facility (UFAFF)¹⁸ to provide a better understanding of landing gear noise. The current work is focused on the partially-dressed closed-cavity nose landing gear (PDCC-NLG) configuration that was tested in the BART tunnel. In the PDCC-NLG configuration, several smaller components, such as hydraulic lines were removed from the actual flight hardware, and the door cavity where the landing gear is stowed during the cruise mode, was closed to create a simpler configuration for testing and code validation. The tests were conducted at Reynolds number of 7.3×10^4 based on the main strut (piston) diameter and a free stream Mach number of 0.166. Transition strips were attached on the model along the length of the strut to produce a turbulent boundary layer prior to flow separation on the strut. No such transition treatment was deemed necessary for the wheels. Detailed steady pressure data is available on the wheels, door and fuselage. In addition, unsteady pressure data was collected at 10 strategically located Kulite pressure transducers. Off-surface particle image velocimetry (PIV) measurements were taken to examine the detailed flow characteristics near critical components. Both phased and linear microphone arrays were used in the UFAFF for collecting noise data away from the landing gear.

III. Governing Equations and Flow Solver

In the present work, a spatially second-order accurate CFD code, FUN3D, is used to obtain numerical solutions of the unsteady Navier-Stokes equations. A hybrid approach is used with the Reynolds-averaged Navier-Stokes (RANS)

equations solved in regions where the grid is inadequate to resolve the unsteady flow features, such as near solid walls, and a Large Eddy Simulations (LES) approach used in remainder of the computational domain. The details of the switch between these regions and the subgrid scale model are dependent on the turbulence model used for simulations.^{19,20}

FUN3D is an unstructured grid flow solver developed originally by Anderson and Bonhaus.²¹ The FUN3D code has gone through significant modifications over the years by a team of researchers at NASA LaRC using modern software practices.¹⁴ The discrete form of the governing equations are solved either in a time-accurate manner with a constant time-step at every grid point or with variable time stepping to accelerate convergence to a steady state. At each iteration step, a linear system of equations is relaxed in a red-black fashion with a point implicit procedure.²² The FUN3D code can accommodate multiple element types including tetrahedrons, prisms, pyramids and hexahedrons, which makes it compatible with many different grid generators. For the current work, Roe's flux-difference splitting scheme²³ is used without a flux limiter.

FUN3D employs a dual time-stepping algorithm with subiterations to converge the solution within each time-step. Between 15-30 subiterations per time-step were used, but the number varied for different cases to obtain at least 3 orders of magnitude reduction in the residuals of governing equations. A variety of time marching schemes are available in FUN3D, including a second-order backward-differencing formulation (BDF2), and an optimized second order backward differencing formulation (BDF2OPT). The BDF2OPT scheme,²⁴ which produces higher temporal accuracy compared to the standard BDF2 scheme at nominally the same computational cost but with slightly increased memory usage was chosen for current applications.

IV. Turbulence Models

It is well known that standard RANS turbulence models, such as the Spalart-Allmaras model²⁵ and the shear stress transport (SST) model of Menter,²⁶ produce overly diffusive unsteady solutions in the presence of large separated flows encountered in the wake regions of bluff bodies. In this paper we make use of two turbulence models that have been shown to accurately capture the turbulent structures observed in wake and reverse flow regions for a variety of configurations. The first model under consideration here is formed by a linear combination of the two-equation SST model²⁶ developed for RANS equations and an LES subgrid scale model as described by Lynch and Smith.¹⁹ This turbulence model is available in the FUN3D code and produced results that were in as good of agreement with the experimental data as other models used in an international workshop examining a tandem cylinder configuration.^{15,27} This model will be referred to as hybrid RANS/LES or "HRLES" model. Such hybrid models are gaining broader acceptance in the CFD community (see Refs. 20, 28, 29) because they directly simulate more of the unsteady flow physics. In addition, these hybrid models are relatively independent of grid topology and, therefore, should be applicable to a wider range of configurations.

Another turbulence model under consideration is based on the one-equation Detached Eddy Simulation (DES) model of Spalart.³⁰ Although the DES model has been used often for solving unsteady separated flows, this model depends too strongly on the grid quality and topology, and can lead to non-physical results with grid refinement in viscous layers. Spalart et al.³¹ have recently modified the DES model to overcome some of the shortcomings related to its grid dependence in a new model named Delayed Detached Eddy Simulation or DDES. The DDES model applies a blending function that varies between 0 for RANS mode and 1 for LES mode to the destruction terms. A slight modification of this model was suggested by Vatsa and Lockard¹⁵ to overcome numerical difficulties in the FUN3D code associated with the non-physical behavior of the eddy-viscosity in the upstream region of cylindrical bodies. In this model, the blending function suggested by Spalart et al.³¹ for the DDES model for the destruction terms is applied to the production terms also, and it will be referred to as the modified DDES, or "MDDES" model, in this paper.

V. Configuration and Grids

The configuration under consideration here is the 1/4-scale high-fidelity replica of a partially-dressed Gulfstream G550 nose landing gear that includes part of the lower fuselage section as installed in the BART tunnel at NASA LaRC.¹⁷ A schematic of the computational domain is shown in Fig. 1, where the computational boundaries are displayed. Tunnel side walls are not displayed in this figure for clarity. A more detailed view of the landing gear is shown in Fig. 2 where the locations of unsteady Kulite pressure transducers are indicated in parenthesis next to the components of the landing gear. A set of three successively finer unstructured tetrahedral grids comprised of approximately 9, 25 and 71 million nodes (54, 150, and 420 million elements) were generated using the VGRID grid generation software.³² For each grid refinement level, the average cell size was reduced by a factor of $\sqrt{2}$ in each coordinate direction. Special attention was paid to grid resolution in the wake and shear-layer regions emanating from the door, cylindrical struts, and wheels of the

gear assembly in order to resolve the associated unsteady flow structures. An additional grid consisting of approximately 47 million nodes (280 million elements) was created from the 25 million node grid in order to provide finer resolution surrounding the pressure transducer 15 (see Fig. 2) by refining the mesh in two regions: the first region lies between the strut and the lower arm (torque arm), whereas the second region is downstream of the lower arm and exterior to the wheel's hub. The grid distributions for the 25 and 47 million node grids at a planar cut passing through the Kulite pressure transducer 15 on the lower arm are compared in Fig. 3.

VI. Results

The computations were performed at a free-stream Mach number of 0.166 and a Reynolds number of 7.3×10^4 based on the main strut (piston) diameter to match the test conditions of the experimental study of Neuhart et al.¹⁷ in the BART tunnel at NASA LaRC. Since the experiments were conducted with transition strips to ensure turbulent separation, the computations were run in a fully turbulent mode. A constant wall temperature based on flat plate adiabatic wall conditions and no-slip conditions were imposed on viscous surfaces, which included the gear, fuselage and tunnel floor. At the inflow plane, total pressure and total temperature corresponding to the wind tunnel conditions were imposed. At the outflow, extrapolation was used for the velocities, and the static pressure based on experimental data was imposed. Inviscid wall conditions were applied on rest of the tunnel walls.

Normally, the CFD code is run in steady mode starting from free-stream conditions to expedite the development of the mean flow, followed by a time-accurate simulation to capture the unsteady behavior of the flow field. The simulations are run over long periods of time for aeroacoustics applications, and care must be taken to ascertain that the numerical solutions are converged well within each time-step sub-iteration loop. In addition, the computational time-step must be chosen carefully such that the temporal errors do not pollute the solution accuracy. The physical time-step for these computations was chosen so that 20 time steps per period were used for a 10 KHz signal. The number of time steps per period being inversely proportional to the frequency, temporal resolution at lower frequencies is much higher.

The unstructured grids created by the VGRID³² unstructured grid generation code consist of purely tetrahedral cells (elements). However, VGRID uses an advancing layer technique to fill the viscous region adjacent to solid walls with semi-structured tetrahedral grids. A pre-processing utility available in the FUN3D software tools was used to combine the tetrahedrons into prismatic elements in viscous regions. The initial set of computations were run on the tetrahedral element grids generated by the VGRID code. Computations were then repeated on the mixed-element grids obtained by recombination of near wall tetrahedral cells into prismatic cells. Based on these comparisons, the mixed-element grids clearly produced more accurate solutions compared to the solutions obtained on pure tetrahedral grids with the same number of nodes. Therefore, the majority of the results presented in this paper are based on computations performed on the mixed-element grids, unless mentioned otherwise.

A typical case was run for about 20,000 time steps in an unsteady mode to purge the initial disturbances out of the computational domain before the temporal averaging of the flow solution was initiated. The solutions were run for at least another 60,000 time steps to achieve statistically converged results. The time-averaged surface pressures obtained with the HRLES turbulence model on different grids are compared with experimentally measured data¹⁷ for the port wheel of the landing gear in Fig. 4(a). In general, the agreement with the experimental data improves as the grid is refined. The results obtained with the MDDES turbulence model on the 25 and 71 million node grids are compared with the HRLES results in Fig. 4(b). The effect of turbulence model on the surface pressure seems to become less significant as the grid is refined, and is very minimal for the finest (71 million node) grid considered here.

Next we examine the pressure distributions on the nose-gear door. Experimental measurements were taken along 9 rows of ports mounted on the door surface. The computed pressures for the 25 and 71 million node grids using the HRLES turbulence model along rows 2-4 are compared with the measured data in Fig. 5. Similar comparisons along rows 5-8 are presented in Fig. 6. Because of the coarseness of the experimental data, it is difficult to ascertain the shape of experimental curves and to draw firm conclusions about these comparisons. In general, the computed pressures compare reasonably well with the measurements in the middle portion of the door, especially for the 25M node grid. There is steep drop in computed pressure levels towards the door edges due to sudden expansion of the flow. It is not clear at this time as to what is causing a downward shift in the computed pressures with increased grid density. One possibility is the difficulty associated with imposing inflow and outflow conditions based on experimental data due to close proximity of upstream boundary to the model. Better resolution of the pressure across the entire domain on finer grids may be exacerbating the incompatibilities in the imposed conditions.

PIV data and computed results for the time-averaged spanwise vorticity, "Z-vort", and 2-D turbulence kinetic energy (2-D TKE), $[1/2(u'^2 + v'^2)]$ in a plane downstream of the mid-section of wheels are shown in Figs. 7 - 8, respectively. The computed spanwise vorticity contours are in good agreement with the measured data. Although the 2-D TKE levels

are overpredicted, the computed values are in good qualitative agreement with the measured data. The grid refinement has only a minor effect on these results.

Next we examine the surface pressure power spectral density (PSD) distributions at different locations on the gear. Computations using the HRLES turbulence model have been run with pure tetrahedral grids as well as with mixed-element grids consisting of prismatic elements near solid surfaces to assess the effect of grid topology (tetrahedral vs. mixed element cells) on the accuracy of numerical solutions. The resulting computational solutions are compared with the experimental data in Fig. 9 at two locations on the door corresponding to Kulite pressure transducers (channels) 3 and 10, and in Fig. 10 at transducers 7 (wheel) and 15 (lower-arm). In general, it is observed that for the grids with same number of nodes, the numerical solutions on mixed element grids are in closer agreement with the experimental data compared to the solutions on pure tetrahedral grids. For example, the computational solutions using 9 million mixed element grids are comparable in accuracy to the 25 million tetrahedral grid solutions. Based on such observations, we present only the mixed element grid results in remainder of this paper.

In the next set of figures, we show the effect of grid refinement on the surface pressure power spectral density distributions. For this set, computational solutions obtained with the HRLES turbulence model on mixed element grids of grid density varying from 9 million to 71 million nodes are compared with the experimental data. The surface pressure power spectral density distributions computed at two locations on the door corresponding to Kulite locations (channels) 3 and 10 are compared with the measured data in Fig. 11. The computed power spectral density levels start deviating sharply from measured values around 500 Hz for the coarsest (9 million node) grid. The agreement with computed results shows significant improvement with grid refinement indicating the need for finer grids to resolve high-frequency signals. At these locations, local enrichment of the grid near the lower-arm and wheels to increase the total grid count from 25 to 47 million nodes has a minimal effect on the spectra. However, the uniformly refined 71 million node results produce higher PSD levels in the higher frequency range, and are in better agreement with the experimental data.

Similar comparisons for Kulite pressure transducers on the wheel and lower-arm are presented in Fig. 12. Once again, the agreement with the experimental data shows significant improvement with grid refinement. For these locations, the locally enriched grid (47 million node, Fig. 3) results are as good as, or better than the globally refined (71 million node) grid case. Thus, an adaptive (automatic or manual) grid scheme can be potentially more efficient at improving numerical accuracy in some critical regions of complex configurations compared to a standard global grid refinement strategy.

In order to study the impact of time-step on the numerical accuracy, simulations were also performed for the 71 million node grid with the time-step reduced by a factor of 2 compared to the baseline cases. The power spectral density distributions obtained with the lower time-step are compared with the baseline computations in Figs. 13 and 14. Based on these comparisons, it is concluded that the effect of halving the time-step from the baseline value is quite small on the surface fluctuations and, therefore, it would have minimal effect on far-field noise.

The computational results with the MDDES turbulence model are also shown in Figs. 13 and 14 at the same transducer locations for the 71 million node grid. The two turbulence models used here, i.e., the HRLES and MDDES models produced very similar results for this case. The main difference is seen for transducers 7 and 15, where slightly higher drop off frequency is obtained with the MDDES model.

VI.A. Farfield Noise

Zawodny et al.¹⁸ have conducted aerodynamic and aeroacoustic testing in the UFAFF tunnel of the same nose landing gear that was tested in NASA Langley's BART tunnel. In their experimental work, Zawodny et al.,¹⁸ placed a series of 11 microphones several wheel diameters underneath the nose gear along the centerline of the gear as shown in Fig. 15. The UFAFF is an open-jet, anechoic facility. The spectra at the microphone locations were corrected to account for shear layer refraction. The effective position of microphone 7 is directly underneath the nose gear, closely representing a flyover direction of 90°.

The pressure fluctuations on the solid surfaces of the landing gear configuration obtained from the FUN3D solutions were used as input to the Ffowcs Williams-Hawkings³³ (FW-H) solver PSU-WOPWOP^{34,35} to predict the far-field noise at locations corresponding to the microphones used in the measurements of Zawodny et al.¹⁸

The predicted 1/3 Octave sound pressure levels (SPL) for microphone 4, which is located downstream of the landing gear wheels, are compared with the experimental data in Fig. 16. FW-H predictions using 25, 47 and 71 million node grid FUN3D solutions obtained with the HRLES turbulence model are included in this figure. For the 71 million node grid, results from the MDDES turbulence model are also shown in this figure. The configuration differences between the BART and UFAFF tunnels make the direct comparison of the predicted noise with the experimental data somewhat ambiguous. In both configurations, the gear on the fuselage was mounted on a flat surface. However, the extent of the mounting surface was different in the two facilities. In the BART, the mounting surface was actually the tunnel floor. The other 3 tunnel walls have no correspondence with the open UFAFF configuration. Because of the reflections from the

walls in the simulated BART configuration, no permeable surface FW-H calculations were attempted. Furthermore, only the solid surface data from the gear, fuselage, and the tunnel wall on which the model was mounted (tunnel-floor) were used in the FW-H predictions. Noise calculations using the gear alone, gear + fuselage, and gear + fuselage + tunnel-floor were performed to assess the effect of different components on the noise. Furthermore, predictions were made with the gear alone and the gear + fuselage mirrored across the tunnel floor. Mirroring should provide the same effect as an infinite, planar acoustically reflective surface. Noise that might be generated by the interaction of flow structures with the reflective surface are not included when mirroring.

In Fig. 16, all of the spectra for the gear alone are generally below the experimental result. Mirroring the gear produces levels that are in better agreement with the measurements. However, including the CFD data for the fuselage and the tunnel-floor in the FW-H predictions results in levels as much as 15 dB above the experimental data. If the fuselage and floor were acting merely as reflective surfaces, the mirrored gear result should have been similar to that of the tunnel-floor + fuselage + gear. The discrepancy could be caused by either interactions of flow structures with the fuselage and tunnel-floor or reflections from other tunnel walls polluting the data on the fuselage and tunnel-floor. In the latter case, all of the FW-H predictions would be inappropriate for comparison with the experiment. An additional FUN3D simulation of an open-jet configuration more closely resembling the UFAFF setup is planned to gain insight into the flow physics associated with the fuselage and floor.

In general, the predicted levels show a steep drop off in SPL at higher frequencies, similar to what was observed in Figs. 11 - 12 for the power spectral density. The drop-off frequency increases with grid refinement, which improves the comparison with measured data for finer grids.

Similar comparisons for microphones 7 and 9 are shown in Figs. 17 and 18, respectively. The overall trends at these locations are similar to the ones observed in Fig. 16. The predictions based on the MDDES model appear to resolve slightly higher frequencies than the HRLES results. Also, the locally enriched grid (47 million nodes) seems to have the most effect on the SPL levels for microphone 9, indicating that the directivity from the lower-arm may peak in the upstream direction.

VII. Concluding Remarks and Future Directions

Numerical simulations have been performed for a partially-dressed closed-cavity nose landing gear configuration corresponding to the experimental set up of BART tunnel at NASA Langley Research Center. A fully unstructured grid flow solver, FUN3D, was used for solving a hybrid RANS/LES form of the governing equations. Results have been presented for a series of successively finer grids with two different turbulence models. Significant improvement in time-averaged surface pressure and power spectral density comparisons with the experimental data is observed with grid refinement. The difference between results obtained with the HRLES and MDDES turbulence models is small. The effect of reducing the time-step by a factor of 2 was also found to be negligible.

Although the computations were performed to simulate the closed wall configuration of the BART tunnel, an attempt was made to estimate the far-field noise generated by the various components of this configuration. Based on these comparisons, it is clear that interactions with tunnel walls have a significant effect on far-field noise. We are currently working on replicating the test set-up of the landing gear configuration tested in the UFAFF open-jet facility in order to obtain a better correlation with the corresponding noise data. An unstructured grid consisting of 146 million nodes (725 million cells) was generated for this simulation. For this grid, the mesh distribution near the nose-gear surfaces is comparable to the 71 million node grid described in the paper. However, this set-up consists of larger computational domain and enriched grid in a conical region from the gear to some of the central microphones, resulting in a larger grid size.

For the open-jet facility simulation, in addition to collecting unsteady data at the solid surfaces, we are also planning to collect unsteady data on a set of permeable surfaces enclosing the gear and mounting assembly. This data will be input into a FW-H code for predicting the far-field noise and will help us in identifying different sources of noise.

VIII. Acknowledgments

This work was supported by NASA's Fundamental Aerodynamics and Integrated Systems Research Programs through the Subsonic Fixed-Wing and Environmentally Responsible Aviation Projects. The authors are deeply indebted to Dr. Eric J. Nielsen of NASA Langley Research Center for providing invaluable guidance and support related to the mixed element capability of FUN3D code. The authors would also like to acknowledge Mr. Michael Wiese of Analytical Sciences and Material, Inc. (currently with Vigyan, Inc.) for generating the grids used in this work.

References

- ¹Khorrami, M. R., Lockard, D. P., Humphreys, Jr., W. M., Choudhari, M. M., and Van de Ven, T., "Preliminary Analysis of Acoustic Measurements from the NASA-Gulfstream Airframe Noise Flight Test," AIAA Paper 2008-2814, May 2008.
- ²Lockard, D. P., Khorrami, M. R., and Li, F., "High Resolution Calculation of a Simplified Landing Gear," AIAA Paper 2004-2887, May 2004.
- ³Spalart, S., Shur, M., Strelets, M., and Travin, A., "Towards Noise Prediction for Rudimentary Landing Gear," IUTAM Symposium on Computational Aero-Acoustics for Aircraft Noise Prediction: ScienceDirect, Vol. 1, pp. 283-292, June 2010.
- ⁴Keating, A., Dethroux, P., Satti, R., Noelting, S., Louis, J., Van de Ven, T., and Vieito, R., "Computational Aeroacoustics Validation and Analysis of a Nose Landing Gear," AIAA Paper 2009-3154, May 2009.
- ⁵Van de Ven, T., Louis, J., Palfreyman, D., and Mendonca, F., "Computational Aeroacoustics Analysis of 1/4 Scale G550 Nose Landing Gear and Comparison to NASA and UFL Wind Tunnel Data," AIAA Paper 2009-3359, May 2009.
- ⁶Noelting, S. and Dethroux, P., "A Hybrid Lattice-Boltzmann/FW-H Method to Predict Sources and Propagation of Landing Gear Noise," AIAA Paper 2010-3976, June 2010.
- ⁷Morton, S., McDamel, D., and Cummings, R., "F-16XL Unsteady Simulations for the CAWAPI Facet of RTO Task Group AVT-113," AIAA Paper 2007-0493, January 2007.
- ⁸Morton, S., Cummings, R., and Kholodar, D., "High Resolution Turbulence Treatment of F/A-18 Tail Buffet," *Journal of Aircraft*, Vol. 44, 2007, pp. 1769-1775.
- ⁹Cummings, R., Morton, S., and McDaniel, D., "Experiences in Accurately Predicting Time-dependent Flows," *Progress in Aerospace Sciences*, Vol. 44, 2008, pp. 241-257.
- ¹⁰Biedron, R. and Lee-Rausch, E., "Rotor Airloads Prediction using Unstructured Meshes and Loose CFD/CSD Coupling," AIAA Paper 2008-7341, August 2008.
- ¹¹Bartels, R., Chwalowski, P., Massey, S., Heeg, J., Wiesemann, C., and Mineck, R., "Computational Aeroelastic Analysis of the Ares Launch Vehicle During Ascent," AIAA Paper 2010-4374, June 2010.
- ¹²Forsythe, J., Strang, W., and Squires, K., "Six Degree of Freedom Computation of the F-15E Entering a Spin," AIAA Paper 2006-858, January 2006.
- ¹³Cameli, F., Lohner, R., and Hanna, S., "VLES Study of Flow and Dispersion Patterns in Heterogeneous Urban Areas," AIAA Paper 2006-1419, January 2006.
- ¹⁴FUN3D Web page: <http://fun3d.larc.nasa.gov>, March 2010.
- ¹⁵Vatsa, V. and Lockard, D., "Assessment of Hybrid RANS/LES Turbulence Models for Aeroacoustics Applications," AIAA Paper 2010-4001, June 2010.
- ¹⁶Rumsey, C., Biedron, R., and Thomas, J., "CFL3D: Its History and Some Recent Applications," NASA TM 112861, May 1997, presented at the Godonov's Method for Gas Dynamics Symposium, Ann Arbor, MI.
- ¹⁷Neuhart, D., Khorrami, M., and Choudhari, M., "Aerodynamics of a Gulfstream G550 Nose Landing Gear Model," AIAA Paper 2009-3152, May 2009.
- ¹⁸Zawodny, N., Liu, F., Yardibi, T., Cattafesta, L., Khorrami, M., Neuhart, D., and Van de Ven, T., "A Comparative Study of a 1/4-scale Gulfstream G550 Aircraft Nose Gear Model," AIAA Paper 2009-3153, May 2009.
- ¹⁹Lynch, C. and Smith, M. J., "Hybrid RANS-LES Turbulence Models on Unstructured Grids," AIAA Paper 2008-3854, June 2008.
- ²⁰Baurle, R. and Edwards, J., "Hybrid Reynolds-Averaged/Large-Eddy Simulations of a Coaxial Supersonic Free-Jet Experiment," AIAA Paper 2009-0129, January 2009.
- ²¹Anderson, W. K. and Bonhaus, D. L., "An Implicit Upwind Algorithm for Computing Turbulent Flows on Unstructured Grids," *Computers and Fluids*, Vol. 23, No. 1, 1994, pp. 1-21.
- ²²Nielsen, E., Lu, J., Park, M., and Darmofal, D., "An Implicit, Exact Dual Adjoint Solution Method for Turbulent Flows on Unstructured Grids," *Computers and Fluids*, Vol. 33, No. 9, 2003, pp. 1131-1155.
- ²³Roe, P. L., "Approximate Riemann Solvers, Parameter Vectors, and Difference Schemes," *Journal of Computational Physics*, Vol. 43, 1981, pp. 357-372.
- ²⁴Vatsa, V., Carpenter, M., and Lockard, D., "Re-evaluation of an Optimized Second Order Backward Difference (BDF2OPT) Scheme for Unsteady Flow Applications," AIAA Paper 2010-0122, January 2010.
- ²⁵Spalart, P. R. and Allmaras, S., "A One-Equation Turbulence Model for Aerodynamic Flows," *La Recherche Aerospatiale*, Vol. 1, No. 1, 1994, pp. 5-21.
- ²⁶Menter, F. R., "Two-equation Eddy-viscosity Turbulence Models for Engineering Applications," *AIAA Journal*, Vol. 32, No. 8, 1994, pp. 1598-1605.
- ²⁷Lockard, D., "Summary of the Tandem Cylinder Solutions from the Benchmark problems for Airframe Noise Computations-I Workshop," AIAA Paper 2011-353, Jan. 2011.
- ²⁸Sanchez-Rocha, M., Kirtas, M., and Menon, S., "Zonal Hybrid RANS-LES Method for Static and Oscillating Airfoils and Wings," AIAA Paper 2006-1256, January 2006.
- ²⁹Frohlich, J. and von Terzi, D., "Hybrid LES/RANS Methods for the Simulation of Turbulent Flows," *Progress in Aerospace Sciences*, Vol. 44, 2008, pp. 349-377.
- ³⁰Spalart, P. R., "Young Person's Guide to Detached-Eddy Simulation Grids," NASA CR-211032, 2001.
- ³¹Spalart, P. R., Deck, S., Shur, M. L., Squires, K. D., Strelets, M. K., and Travin, A., "A New Version of Detached-Eddy Simulation, Resistant to Ambiguous Grid Densities," *Theoretical and Computational Fluid Dynamics*, Vol. 20, 2006, pp. 181-195.
- ³²Pirzadeh, S., "Three-dimensional Unstructured Viscous Grids by the Advancing Layer Method," *AIAA Journal*, Vol. 33, No. 1, 1996, pp. 43-49.
- ³³Ffowcs Williams, J. E. and Hawkins, D. L., "Sound Generation by Turbulence and Surfaces in Arbitrary Motion," *Philosophical Transactions of the Royal Society of London A*, Vol. 342, 1969, pp. 264-321.
- ³⁴Brentner, K. S., Lopes, L. V., Chen, H. N., and Horn, J. F., "Near Real-Time Simulation of Rotorcraft Acoustics and Flight Dynamics," 59th Annual Forum, AHS International, Alexandria, VA, 2003.
- ³⁵Bres, G. A., Brentner, K. S., Perez, G., and Jones, H. E., "Maneuvering Rotorcraft Noise Prediction," *Journal of Sound and Vibration*, Vol. 275, No. 3-5, 2004, pp. 719-738.

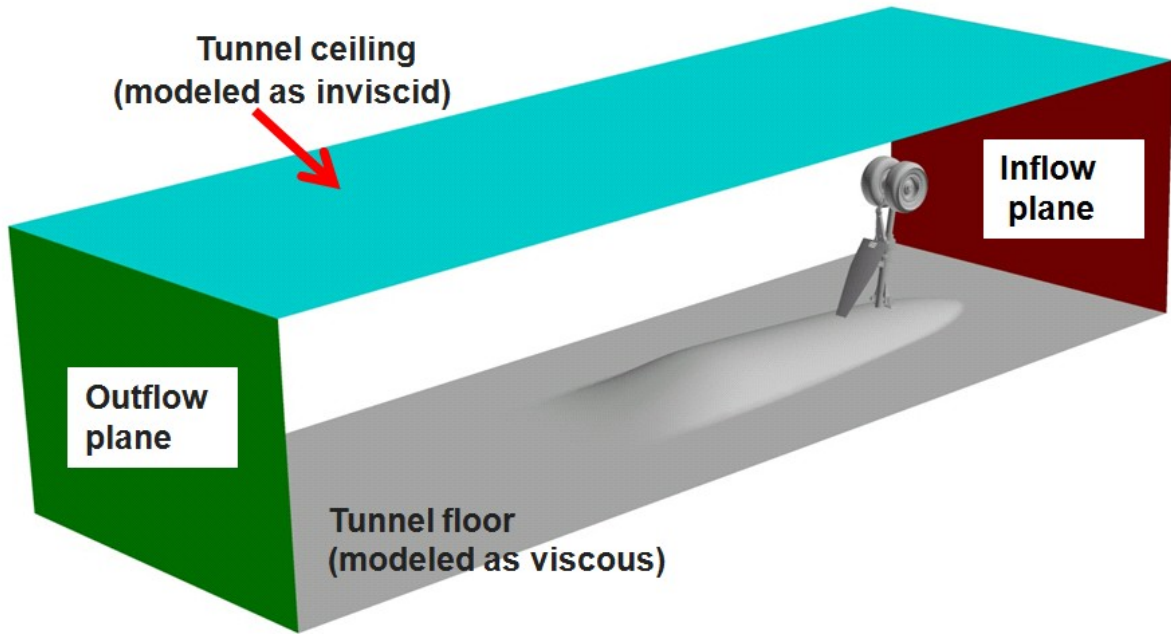


Figure 1. Computational model of the nose landing gear in BART tunnel

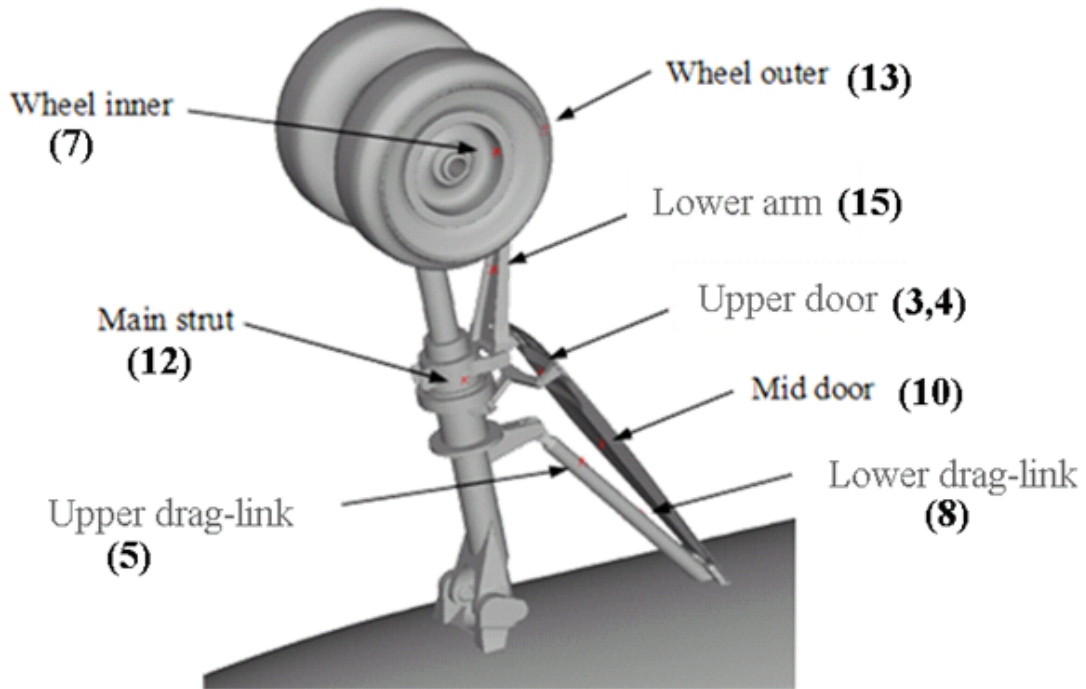


Figure 2. Kulite pressure transducer locations and nomenclature for nose landing gear: Transducer numbers are given in parentheses

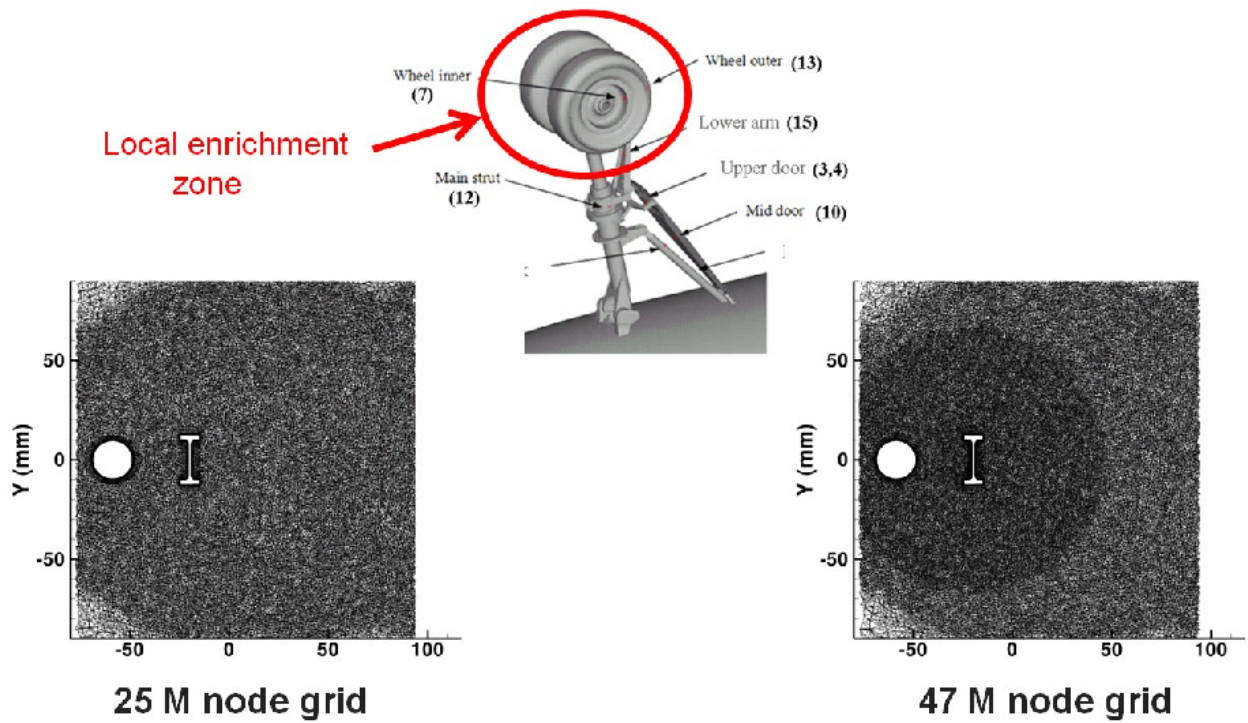


Figure 3. Comparison of baseline and enriched grids at a planar cut through transducer 15 on lower arm

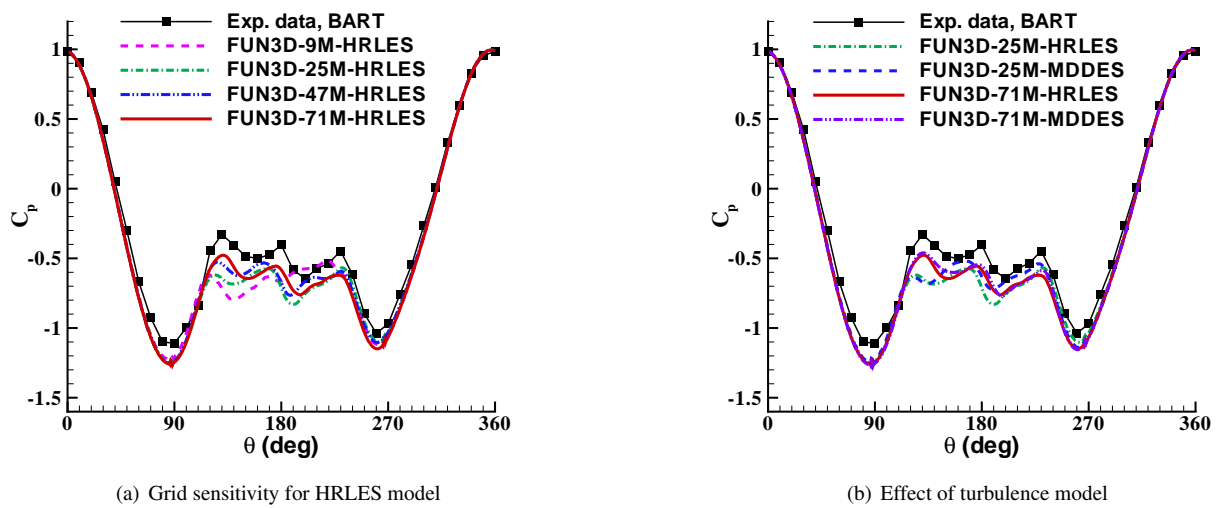


Figure 4. Surface pressure distributions on port wheel

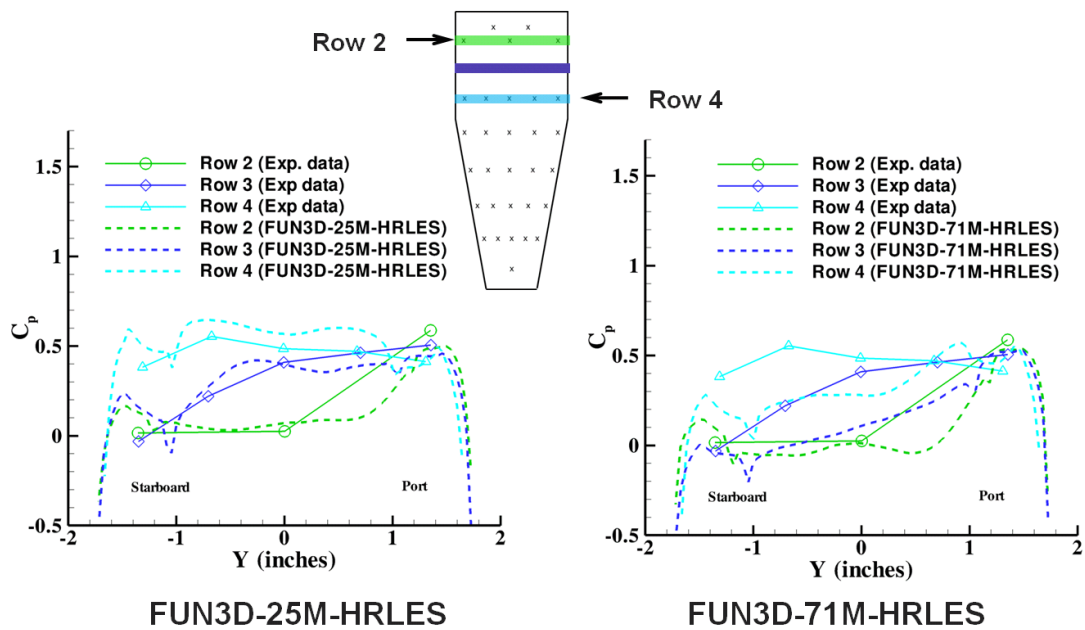


Figure 5. Surface pressure distributions on door, rows 2-4

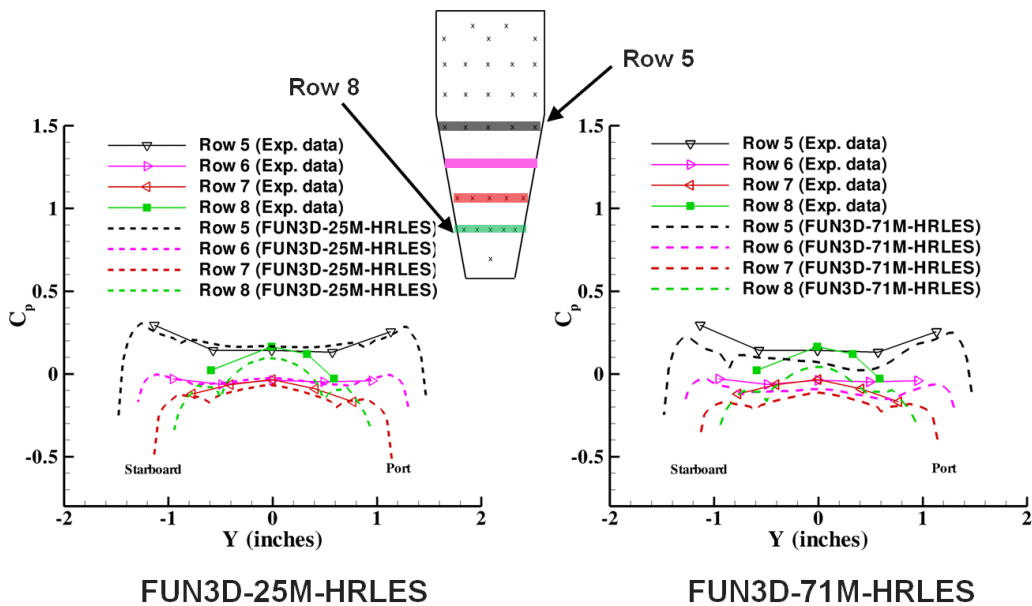


Figure 6. Surface pressure distributions on door, rows 5-8

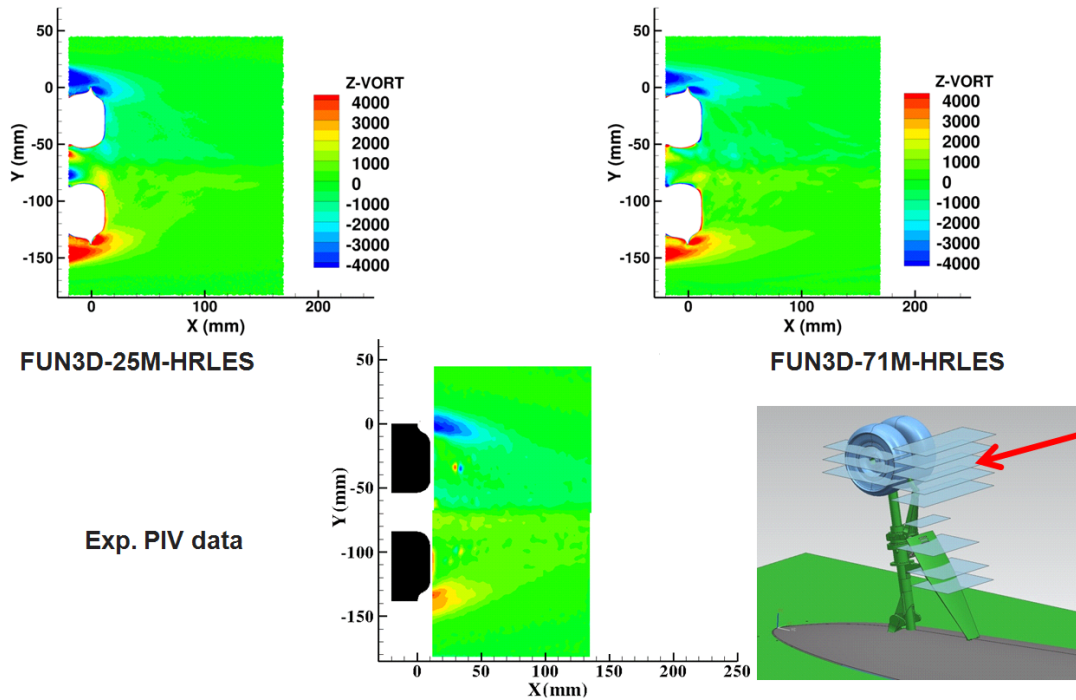


Figure 7. Spanwise vorticity contours, mid-wheel plane

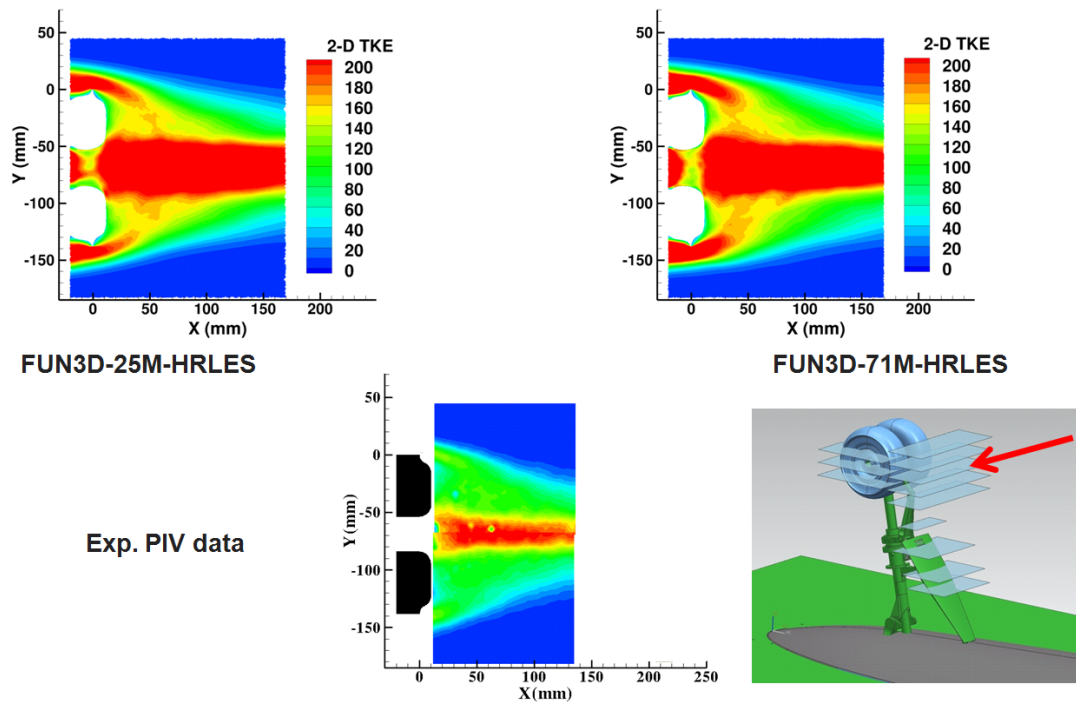


Figure 8. 2-D Turbulence kinetic energy contours, mid-wheel plane

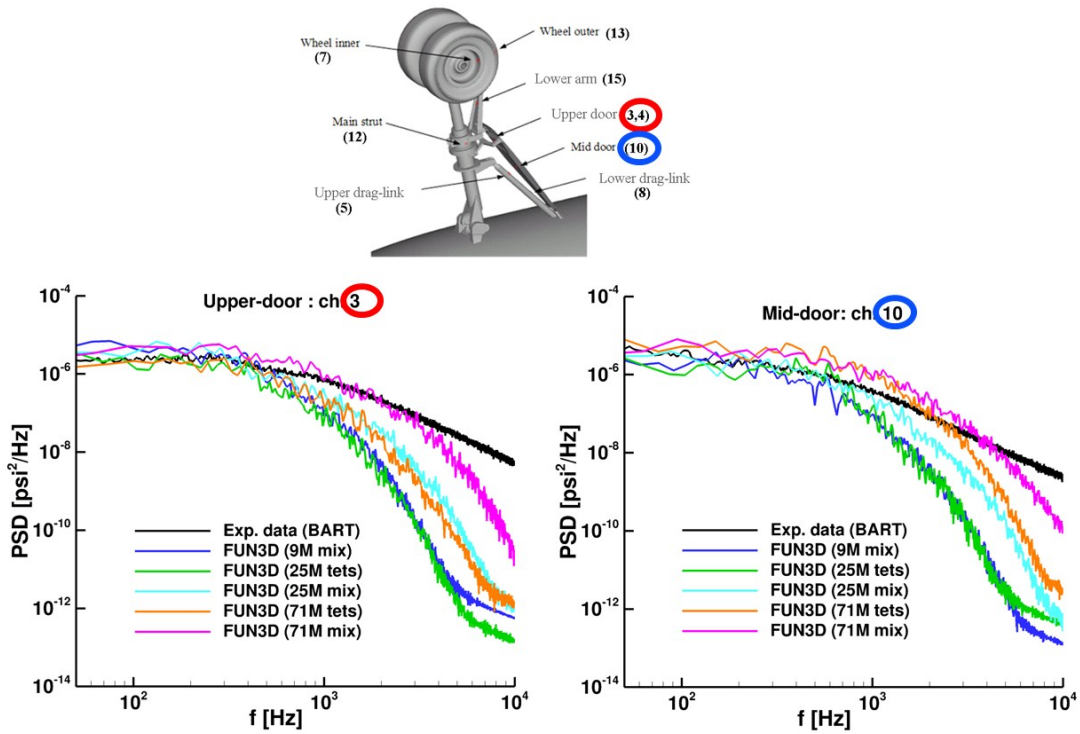


Figure 9. PSD comparisons for Kulite transducers 3 and 10: mixed element vs. tetrahedral grids, HRLES model

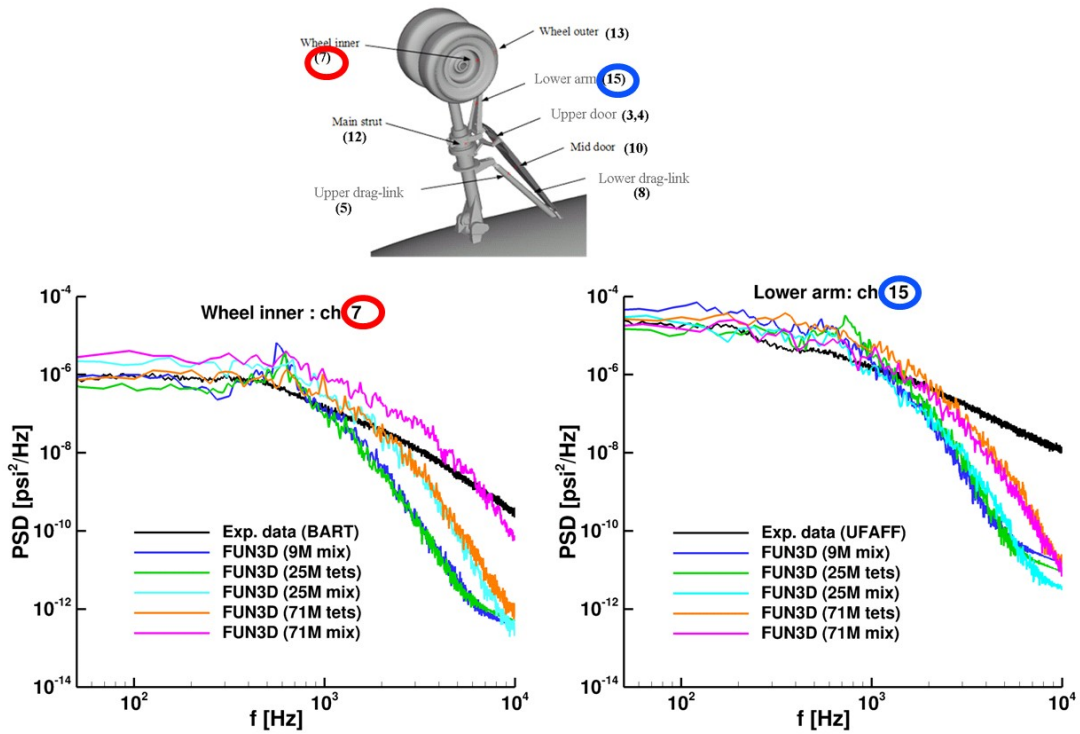


Figure 10. PSD comparisons for Kulite transducers 7 and 15: mixed element vs. tetrahedral grids, HRLES model

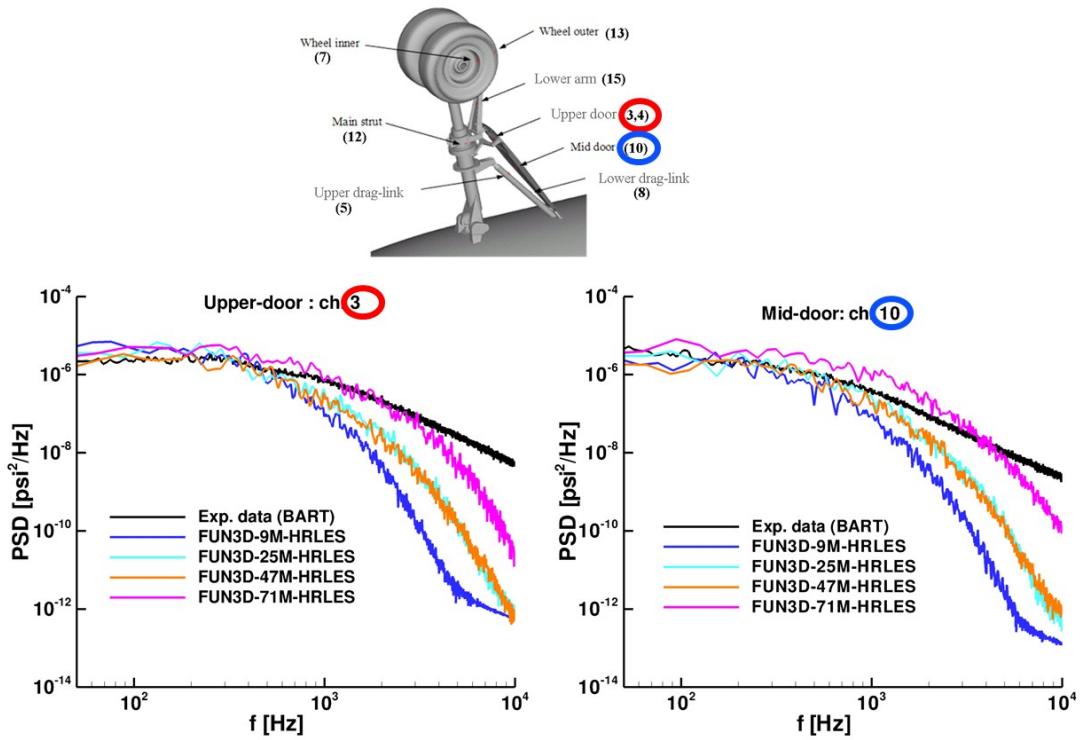


Figure 11. Effect of grid refinement on PSD for Kulite transducers 3 and 10: mixed element grids, HRLES model

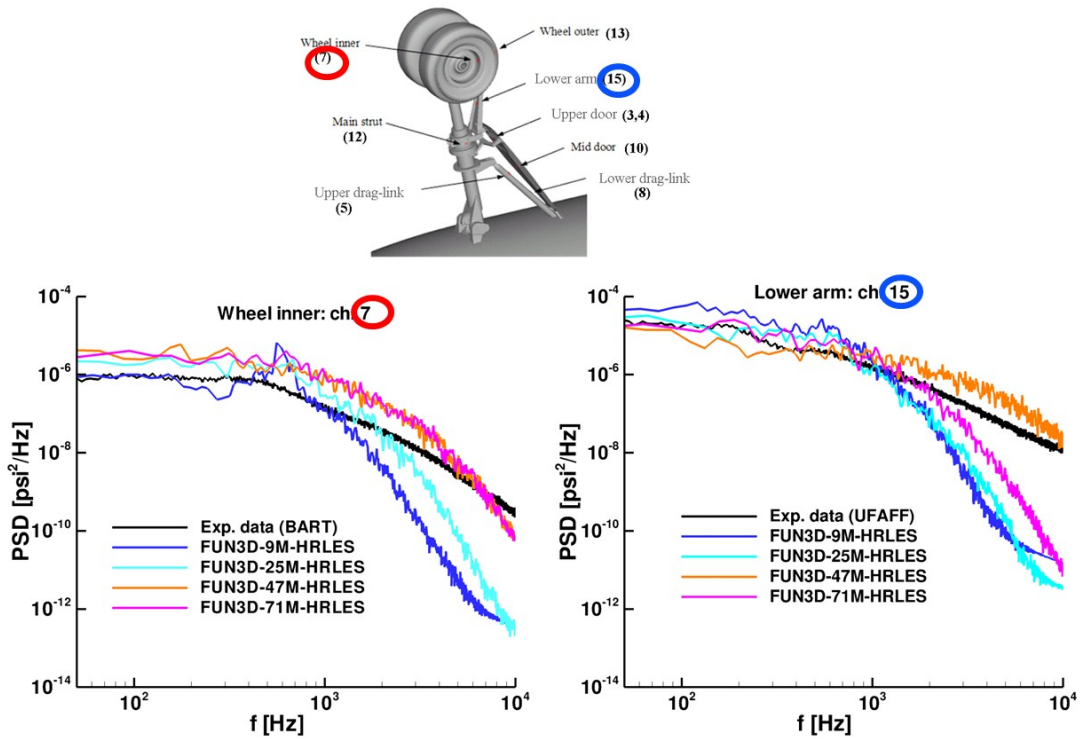


Figure 12. Effect of grid refinement on PSD for Kulite transducers 7 and 15: mixed element grids, HRLES model

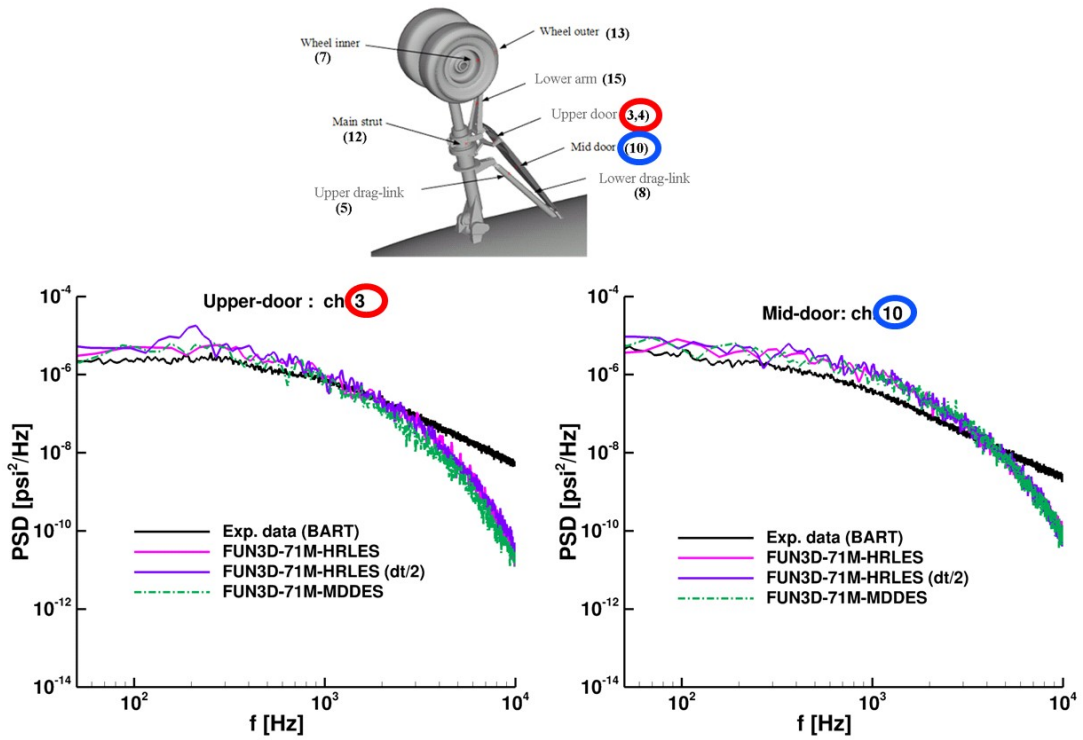


Figure 13. Effect of time-step and turbulence model on PSD for Kulite transducers 3 and 10: 71 M mixed element grid

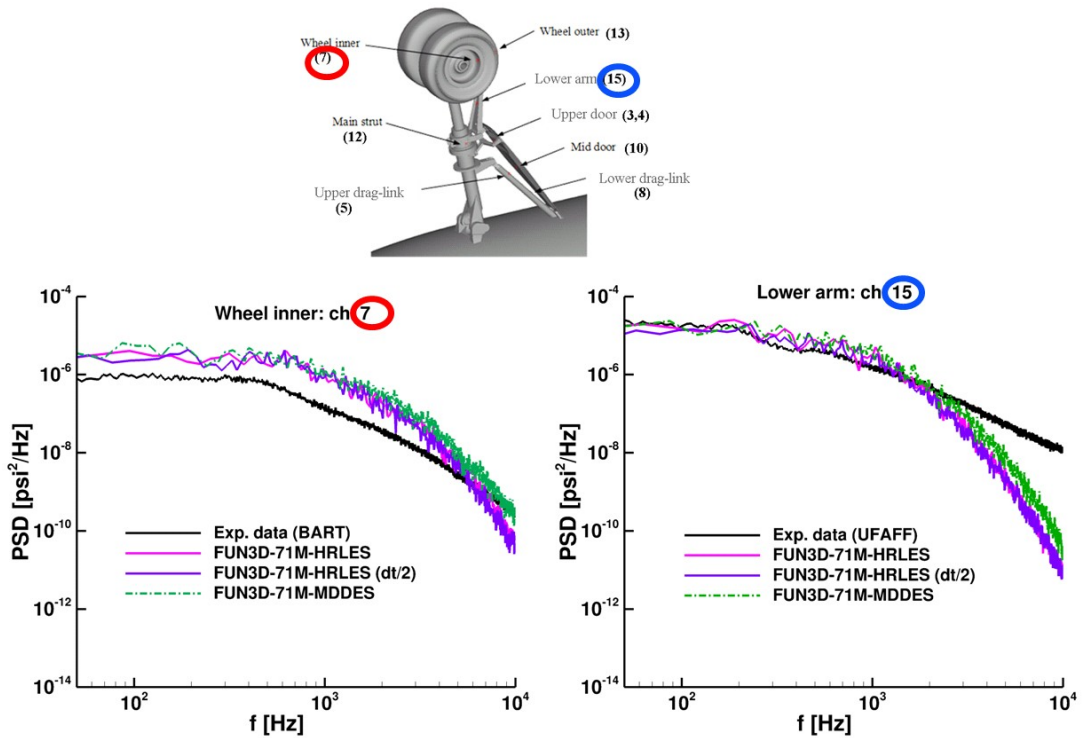


Figure 14. Effect of time-step and turbulence model on PSD for Kulite transducers 7 and 15: 71 M mixed element grid

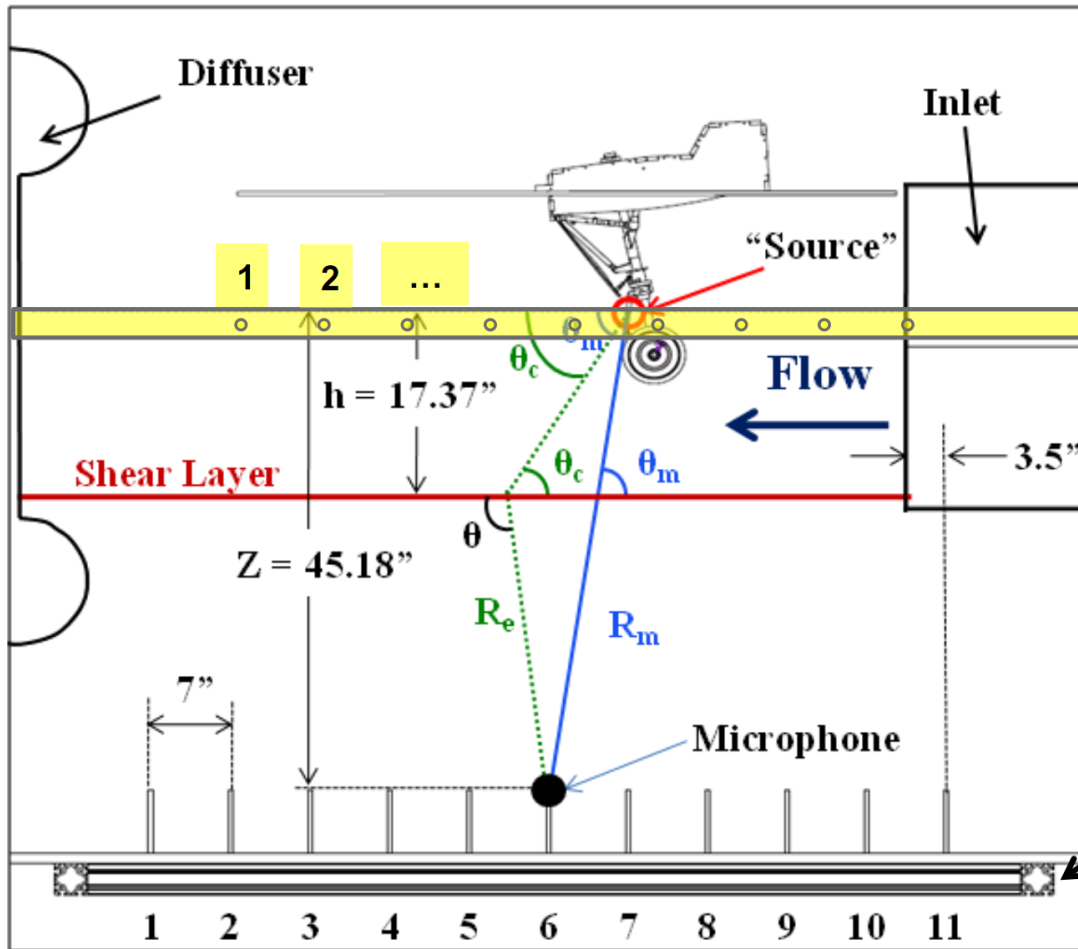
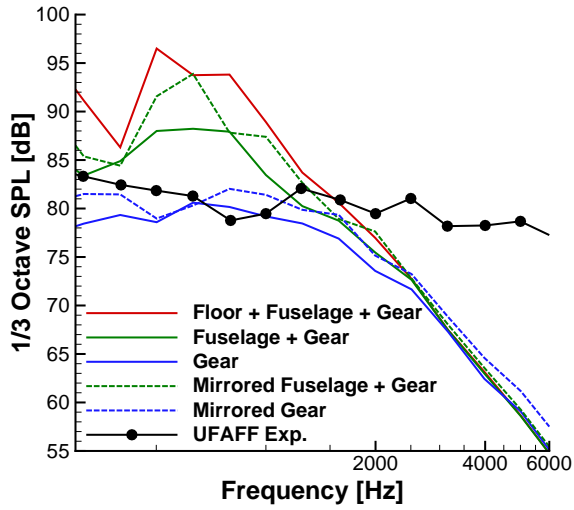
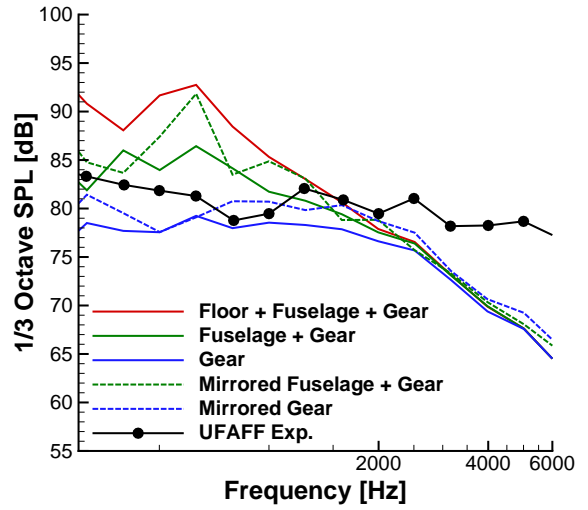


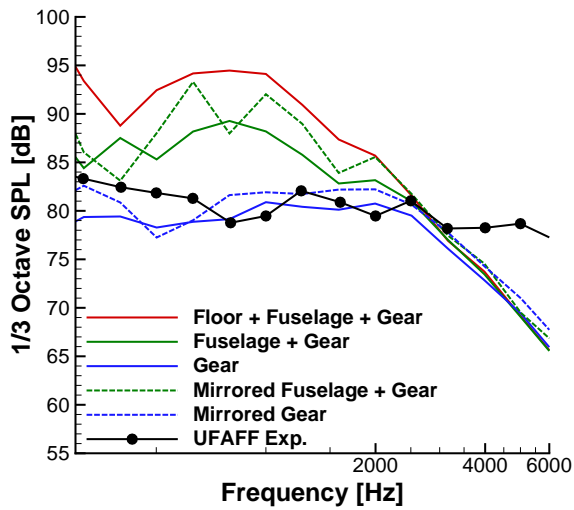
Figure 15. Linear microphone array arrangement in UFAFF



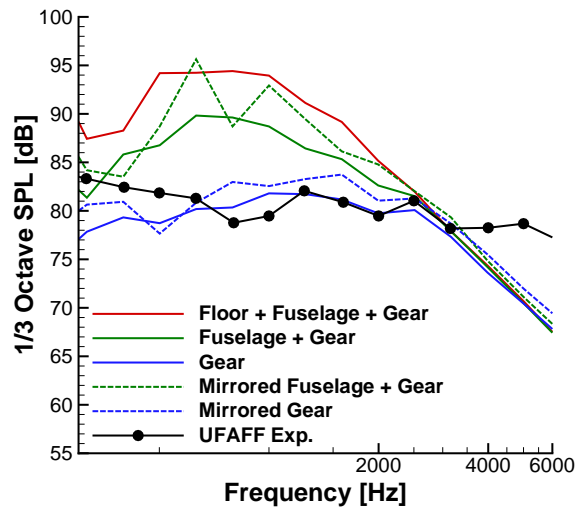
(a) HRLES, 25 M node grid



(b) HRLES, 47 M node grid

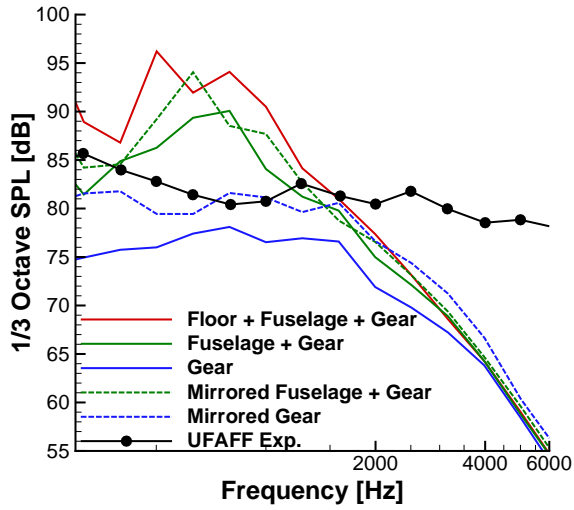


(c) HRLES, 71 M node grid

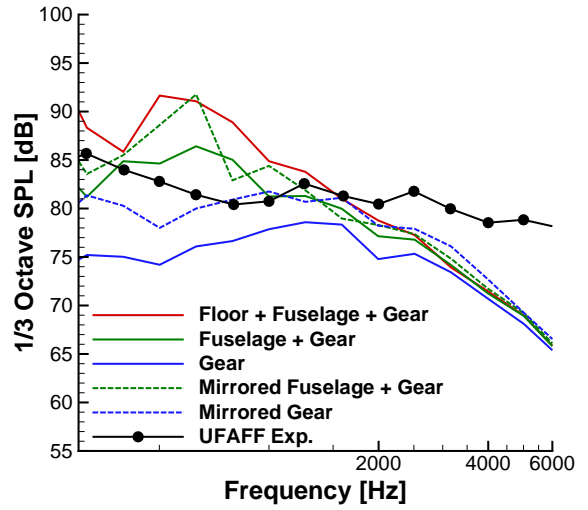


(d) MDDES, 71 M node grid

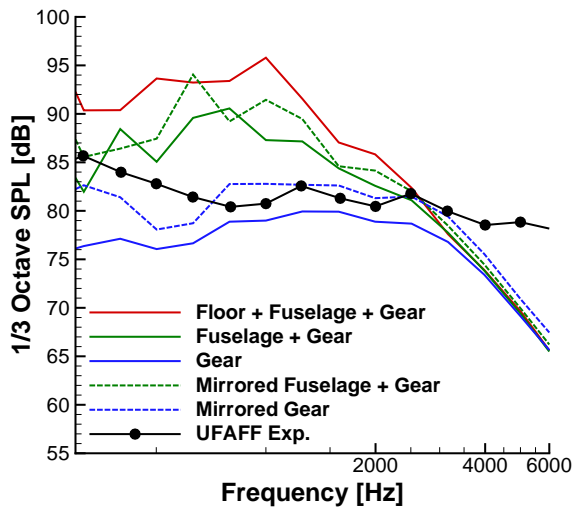
Figure 16. Sound pressure level comparisons, flyover mic 4



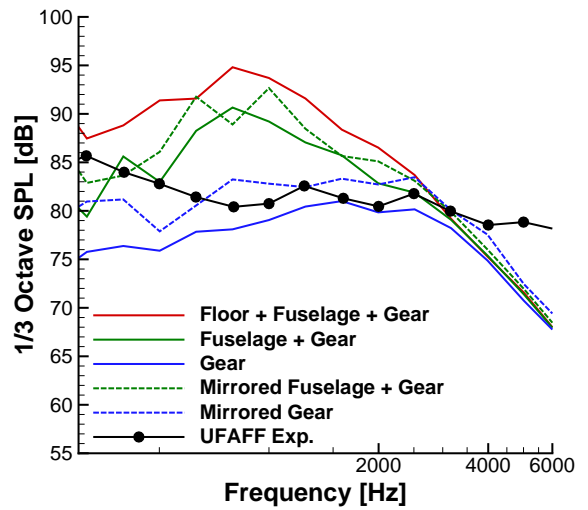
(a) HRLES, 25 M node grid



(b) HRLES, 47 M node grid

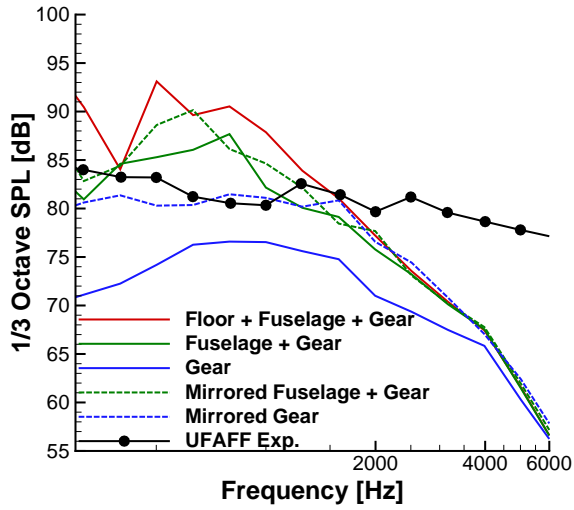


(c) HRLES, 71 M node grid

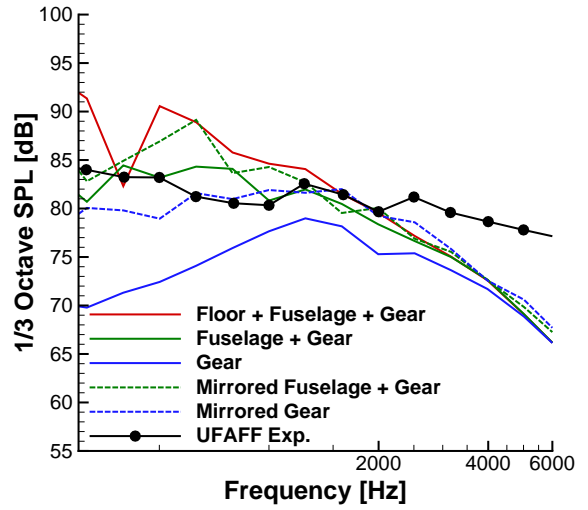


(d) MDDES, 71 M node grid

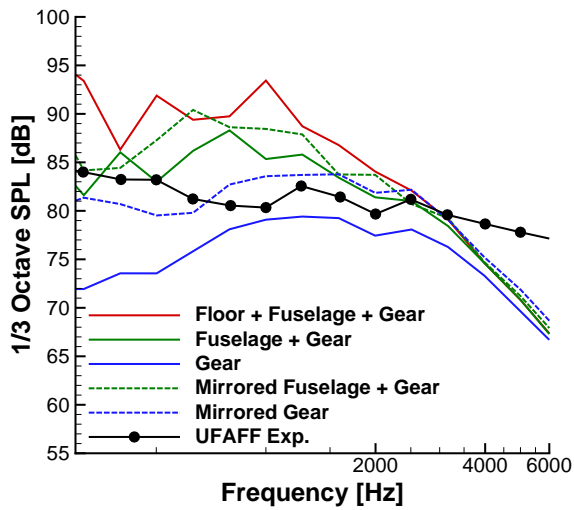
Figure 17. Sound pressure level comparisons, flyover mic 7



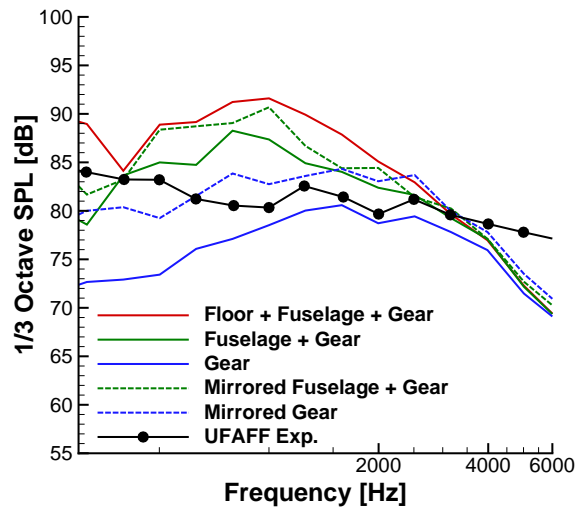
(a) HRLES, 25 M node grid



(b) HRLES, 47 M node grid



(c) HRLES, 71 M node grid



(d) MDDES, 71 M node grid

Figure 18. Sound pressure level comparisons, flyover mic 9